

Exploring Ca^{2+} Dynamics in Myelinating Oligodendrocytes through rAAV-Mediated jGCaMP8s Expression in Developing Spinal Cord Organ Cultures

 Maria Pachetti,*  Anabela Palandri,* Fernanda de Castro Reis,
 Luca Recupero, and Laura Ballerini

Scuola Internazionale Superiore di Studi Avanzati, Trieste 34146, Italy

Received Dec. 19, 2023; revised April 15, 2024; accepted April 16, 2024.

The authors declare no competing financial interests.

Author contributions: M.P., A.P., and L.B. designed research; M.P., A.P., F.d.C.R., and L.R. performed research; M.P. and A.P. analyzed; M.P., A.P., and L.B. wrote the paper.

We thank Prof. Paul Heppenstall and Prof. Andrea Nistri for their critical revision of the paper and for their helpful discussions. We also thank Mario Fontanini for the imaging technical assistance. This work was supported by the Italian Ministry for Scientific Research (MIUR), PRIN 2022 (2022CFSE5S). M.P. was supported by the PRO3 fellowship (DM No. 2503, dd. 09/12/2019), and A.P. was supported by the Human Frontier Science Program grant RGP0004/2019 and European Union Horizon 2020 Research and Innovation Programme under grant agreement no. GrapheneCore3 (881603).

*M.P. and A.P. contributed equally to this work.

Correspondence should be addressed to Maria Pachetti at mpachett@sissa.it or Laura Ballerini at ballerini@sissa.it.

Copyright © 2024 Pachetti et al. This is an open-access article distributed under the terms of the [Creative Commons Attribution 4.0 International license](https://creativecommons.org/licenses/by/4.0/), which permits unrestricted use, distribution and reproduction in any medium provided that the original work is properly attributed.

Abstract

Oligodendrocytes, the myelin-producing glial cells of the central nervous system (CNS), crucially contribute to myelination and circuit function. An increasing amount of evidence suggests that intracellular calcium (Ca^{2+}) dynamics in oligodendrocytes mediates activity-dependent and activity-independent myelination. Unraveling how myelinating oligodendrocytes orchestrate and integrate Ca^{2+} signals, particularly in relation to axonal firing, is crucial for gaining insights into their role in the CNS development and function, both in health and disease. In this framework, we used the recombinant adeno-associated virus/Olig001 capsid variant to express the genetically encoded Ca^{2+} indicator jGCaMP8s, under the control of the myelin basic protein promoter. In our study, this tool exhibits excellent tropism and selectivity for myelinating and mature oligodendrocytes, and it allows monitoring Ca^{2+} activity in myelin-forming cells, both in isolated primary cultures and organotypic spinal cord explants. By live imaging of myelin Ca^{2+} events in oligodendrocytes within organ cultures, we observed a rapid decline in the amplitude and duration of Ca^{2+} events across different in vitro developmental stages. Active myelin sheath remodeling and growth are modulated at the level of myelin–axon interface through Ca^{2+} signaling, and, during early myelination in organ cultures, this phase is finely tuned by the firing of axon action potentials. In the later stages of myelination, Ca^{2+} events in mature oligodendrocytes no longer display such a modulation, underscoring the involvement of complex Ca^{2+} signaling in CNS myelination.

Key words: adeno-associated virus; calcium; live imaging; myelinating oligodendrocytes; spinal cord organ cultures

Significance Statement

Determining the sources and mechanisms driving Ca^{2+} events in mature oligodendrocytes, typically studied through restricted transgenic lines, has proven to be challenging. To address this, we employed the recombinant adeno-associated virus/Olig001 to selectively express jGCaMP8s, under the transcriptional control of the myelin basic protein promoter, to monitor Ca^{2+} activity specifically in myelinating and mature oligodendrocytes in vitro and ex vivo. Our findings indicate that Ca^{2+} dynamics undergoes maturation-dependent modulation and that neuronal activity can have a different impact on Ca^{2+} activity across developmental stages. Our research introduces a valuable genetic tool for monitoring Ca^{2+} signaling in myelin-forming cells to investigate how Ca^{2+} regulation affects oligodendrocyte function and dynamic interactions with axons.

Introduction

Glial cells are key modulators of neural network formation and function (Allen and Lyons, 2018). Among these, oligodendrocytes, the CNS myelinating glia, extend segments of the

lipid-rich myelin membrane in between nodes of Ranvier on numerous axons, facilitating rapid saltatory action potential conduction. Myelinating cells are adaptable and dynamically regulate the number, distribution, length, and thickness of myelin sheaths in response to neuronal activity (Paez and Lyons, 2020). Myelinating oligodendrocytes play a crucial function in providing metabolic support to axonal processes, and altered or dysfunctional axon–glia coupling can lead to neuronal/axonal degeneration (Monje, 2018). Dynamic interactions between myelinating oligodendrocytes and axons include ion homeostasis, regulated by channels localized in the myelin sheath at the axon–myelin interface. As a ubiquitous signaling molecule and second messenger, the dynamic of intracellular Ca^{2+} concentration ($[\text{Ca}^{2+}]_i$) in oligodendrocytes can directly influence the formation and remodeling of myelin and may underlie other, yet unknown, cellular functions (Giorgi et al., 2018; Paez and Lyons, 2020).

During development, the modulation of $[\text{Ca}^{2+}]_i$ affects various aspects of oligodendrocyte progenitor cell (OPC) maturation (Wake et al., 2011), including their differentiation and the myelin sheath formation and growth (Baraban et al., 2018; Krasnow et al., 2018; Bettefeld et al., 2019). On the other hand, demyelination occurs in the immune-mediated disease multiple sclerosis, and it is commonly seen in traumatic brain injury, spinal cord injury, stroke, and aging (Chen et al., 2020). Activation of Ca^{2+} channels and receptors in OPCs and oligodendrocytes by neurotransmitters converges to regulate $[\text{Ca}^{2+}]_i$, making Ca^{2+} a signaling crossroad and a central candidate mediator tuning myelination (Paez and Lyons, 2020). Transgenic animal models, ad hoc modified to express genetically encoded Ca^{2+} indicators (GECIs), are conventionally used for studying Ca^{2+} signaling in mammalian oligodendrocytes (Lu et al., 2023). Although these models have provided valuable insights, they have substantial limitations, including costly breeding schemes and financial and animal welfare concerns, and are generally limited to one gene target at a time. Furthermore, relying on transgenic GECI-expressing lines restricts the flexibility to adopt new generations of GECIs with enhanced performance (Grødem et al., 2023).

This study introduces a recombinant adeno-associated virus (rAAV) to achieve robust expression of targeted GECIs in myelinating oligodendrocytes. By integrating the recently developed jGCaMP8s, with enhanced sensitivity and kinetics (Zhang et al., 2023), with the chimeric AAV/Olig001 capsid variant, which exhibits a preferential tropism for oligodendrocytes in vivo (Powell et al., 2016), our AAV-pMBP-jGCaMP8s-WPRE viral vector emerges as a potent and innovative tool. We show the vector efficiency in reporting live imaging of intracellular Ca^{2+} dynamics specifically and selectively in myelinating oligodendrocytes, with sustained expression persisting for >2 weeks in spinal cord organotypic slices. Leveraging our knowledge of the molecular regulators of Ca^{2+} in other cells, including neurons and astrocytes, we are now beginning to understand the factors converging on the regulation of Ca^{2+} in oligodendrocytes during distinct stages of myelination. The ability to localize jGCaMP8s in myelinating oligodendrocytes provides the possibility to uncover the nature of Ca^{2+} signaling within and between cells.

Materials and Methods

Mice husbandry. All animal studies were carried out with approval of the European Union (EU) and Italian Ministry of Health according to its regulations, under guidelines 2010/63/UE and Decree 26/14. The project was approved by SISSA Animal Care and Use Committee. Animal use was approved by the Italian Ministry of Health 22DABN1WO and 22DABNYQA, in agreement with the EU Recommendation 2007/526/CE.

Organotypic spinal cord cultures. Organotypic spinal cord and dorsal root ganglia slices were obtained from C57BL/6J mouse embryos at Embryonic Day 12.5. Pregnant mice were exposed to a CO_2 overdose and decapitated, and fetuses were delivered by cesarean section. Isolated fetuses were decapitated, and their backs were isolated from low-thoracic and high-lumbar regions and transversely sliced with a tissue chopper. Slices (275 μm) were cleaned by dissection, fixed on a glass coverslip with fibrin glue, that is, reconstituted chicken plasma (Rockland Immunochemicals) clotted with thrombin (Merck Millipore) and cultured within flat-bottom 15 ml screw cap tubes containing 1 ml standard Dulbecco's modified Eagle's medium (DMEM; Thermo Fisher Scientific) supplemented with 25% fetal bovine serum (FBS; Thermo Fisher Scientific), B27 (Thermo Fisher Scientific), 50 units/ml penicillin–streptomycin (Invitrogen), and mouse nerve growth factor (10 ng/ml, Alomone Labs). The tubes were placed in a roller drum, which rotated at a rate of 120 rpm, at 37°C with 5% CO_2 . Experiments were performed on Day In Vitro 14 (DIV14) and DIV21.

OPC isolation and oligodendrocytes cultures. OPC cultures were generated from 0- to 3-d-old Wistar rat pups using a modified protocol from Dai et al. (2014). The mixture was placed into poly-L-ornithine-coated 75 cm^2 flasks and grown in DMEM high glucose (Thermo Fisher Scientific) with 10% FBS for 10–12 d. OPCs were purified from mixed glial cells by a shake-off procedure. Microglia were removed by shaking (100 rpm, 1 h, 37°C); the medium was replaced, and OPCs were purified by shaking overnight (ON; 210 rpm, 37°C). The medium containing cells was collected and filtered (pore size, 70 μm) into noncoated Petri dishes for attachment of astrocytes (1 h). Then, OPCs were centrifuged at 1,200 \times g for 5 min, and cells were resuspended in a medium containing DMEM, 100 \times oligodendrocyte supplement (DMEM, 10.2 mg/ml BSA, 6 μg /ml progesterone, 1.61 mg/ml putrescine, 500 ng/ml sodium selenite, 2.5 μg /ml insulin, 200 mM L-glutamine, 50 μg /ml holo-transferrin, 1 \times N2; Thermo Fisher Scientific) plus 10 ng/ml PDGF and FGF. Cells were cultured in a humidified incubator with 5% CO_2 , with medium changed every 2 d. To initiate differentiation, we shifted the cells to

mitogen-free N2 media plus 15 nM triiodothyronine (T3, Sigma-Aldrich). For calcium imaging assays, 1×10^5 cells/cover-slip were plated in poly-D-lysine-coated coverslips (12 × 24 mm).

Immunofluorescence and confocal microscopy. Cells and spinal cord tissues grown on glass coverslips were washed twice with phosphate-buffered saline (PBS) and fixed with 4% (w/v) paraformaldehyde (Sigma-Aldrich), in PBS for 10 or 30 min at room temperature (RT), respectively. After three washes with PBS, the cells/tissues were incubated for 1 h at RT with a 5% (v/v) solution of goat serum in PBS permeabilized with 0.3% (w/v) Triton X-100 (TX110; Sigma-Aldrich). Samples were incubated with primary antibodies ON in a 5% (v/v) solution of goat serum in PBS with 0.3% (w/v) Triton X-100. After three washes with PBS, cells/tissues were incubated for 2 h at RT with secondary antibodies. Following three washes with PBS, cell nuclei were stained with 4',6-diamidino-2-phenylindole (DAPI) dye (Invitrogen). The coverslips were mounted using Fluoromount-G Mounting Medium (Invitrogen). Confocal images were acquired using a Nikon A1R confocal microscope (Nikon), equipped with 4× (NA 0.20), 20× (NA 0.75), and 40× (NA 0.95) air objectives and 60× (1.35 NA) oil immersion objective. Images (1,024 × 1,024 pixels) were processed using the Fiji ImageJ software. The final images were compiled using the Adobe Photoshop CC software. The following primary antibodies were used: rabbit anti-Ibal (1:500, MA5-36257, Invitrogen); mouse anti-GFAP (1:1000, G3893, Sigma-Aldrich), rabbit anti-myelin basic protein (MBP; 1:1000, ab40390, Abcam), and mouse anti-SMI-32 (1:1000, 801701, BioLegend). Secondary antibodies used were as follows: Alexa Fluor 633 goat anti-mouse, Alexa Fluor 633 goat anti-rabbit, Alexa Fluor 594 goat anti-rabbit, and Alexa Fluor 594 goat anti-mouse (1:1000, Invitrogen). Propidium iodide (PI; Sigma-Aldrich) was used at 5 µg/ml in the culture medium to label dead cells in spinal cord organotypic slice cultures.

Plasmid construct. A plasmid containing the jGCaMP8s and the woodchuck hepatitis virus posttranscriptional regulatory element (WPRE) flanked by AAV2 inverted terminal repeats was used as a recipient plasmid (Addgene). It was digested by Apal and BamHI-HF to replace the human synapsin promoter with the 1.9 kb MBP gene promoter, amplified by PCR from the plasmid (Addgene; FW, atgctctaggaagatctctgcagagggccgagctcctcctgcttaggc; RV, tgatgatggtgat-gatgcatggtggcggtggatcctattcgactccggaagctg; Sigma-Aldrich; Table 1). To generate AAV-MBP-jGCaMP8s-WPRE, we performed a Gibson Assembly reaction by combining the digested backbone with the amplified MBP promoter (insert, backbone; ratio, 3:1 w/w). The resulting vector was validated by sequencing (detailed data reported in Extended Data Table 1-1).

Virus production. The AAV production protocol was adapted from Chakrabarti et al. (2020). Briefly, HEK293T cells, obtained from American type Culture Collection, were cultured in DMEM (Thermo Fisher Scientific) supplemented with 10% FBS and 100 units/ml penicillin–streptomycin (Invitrogen) using a two-culture chambers CellSTACK (Corning). At each passage, cells were trypsinized for 1–3 min with 0.25% trypsin and 1 mM EDTA in PBS, pH 7.4 at 37°C, plated, and maintained for 2 d before transfection. Then, cells were triple transfected with the following plasmids: AAV-MBP-jGCaMP8s-WPRE (cargo) and helper and Rep/Cap Olig001 (Addgene) in a 1:2:1 (w/w) ratio using a linear poly-ethylenimine (PEI) reagent (Polysciences), at 0.33 mg/ml (1:11 plasmid:PEI w/v; Table 1). Three days after transfection, cells and media were harvested and treated with Triton X-100 and RNase A (Sigma-Aldrich) to a final concentration of 0.5% and 5 µg/ml, respectively, shaking for 1 h at 37°C. This mixture was centrifuged at 3,700 × g at RT for 30 min to remove debris and then concentrated by tangential flow filtration using the Vivaflo 200 cassette 100 kDa molecular weight cutoff (MWCO; Sartorius).

The concentrated medium containing rAAV particles was purified through an iodixanol column (OptiPrep density gradient medium; Serumwerk Bernburg) by ultracentrifugation (Optima XE-90 Ultracentrifuge; Beckman Coulter) at 44,400 rpm for 2 h at 18°C. After collecting the 40% layer, rAAV particles were further concentrated using a 50 kDa MWCO filter (Amicon, ultracentrifugal filters), followed by buffer exchange to 0.001% PBS–pluronic

Table 1. A comprehensive list of plasmids, primers, and probes used in this work

Vector name	Addgene no.
pGP-AAV-syn-jGCaMP8s-WPRE	162374
AAV_pMBP-EGFP-caax	190155
pAdDeltaF6	112867
Olig001	170716
Primers and Probes	Sequence
MBP (FW)	5'-CAGAGACACGGGCATCCTTG-3'
MBP (RV)	5'-GTGTGTGAGTCCTTGCCAGAG-3'
MBP probe	5'-TxRd-TCCATCGGGCGCTTCTTTAGCGGTGACA-BHQ2-3'
GAPDH (FW)	5'-TTCAAGTGGGCCCGG-3'
GAPDH (RV)	5'-GTGAGGCCGGTGCTGAGTAT-3'
GAPDH probe	5'-Cy5.5-ATGGTGGTGAAGACACCAGTAGACTCCACG-BHQ3-3'

acid 200 mM NaCl solution. Viral titers (vg/ml) were measured by probing for inverted terminal repeats (FW, GGAACCCCTAGTGATGGAGTT; RV, CGGCCTCAGTGAGCGA) with quantitative polymerase chain reaction (qPCR) using a SsoAdvanced Universal SYBR Green Supermix (Bio-Rad Laboratories), according to the manufacturer's instructions. The protocol was optimized to produce rAAVs at high titer [$\geq 5 \times 10^{14}$ vector genomes (vg/ml)]. Due to the extensive virus's nomenclature, both the following text and images designate it as AAV-mbp:jGCaMP8s.

Quantification of AAV:mbp-jGCaMP8s transduction efficiency. The quantification of the viral expression efficiency was assessed using the "Analyze particles" function in the Fiji ImageJ software, employing Z-stacks of 20× or 40× images obtained from both the oligodendrocyte dissociated culture and the ventral horn of the spinal organ cultures at DIV14 and DIV21. This function identifies colocalization between eGFP+ cells and MBP+ cells, targeting transduced myelinating oligodendrocytes.

Live calcium imaging. For in vitro live calcium imaging, Oregon Green 488 BAPTA-1 AM (Invitrogen) and AAV-mbp:jGCaMP8s were employed. Primary cultures of oligodendrocytes were incubated with 4 μ M Oregon Green 488 BAPTA-1 AM for 40 min (37°C; 5% CO₂; Rauti et al., 2020) or infected at DIV4 (at a final concentration of 2.3×10^8 vg in 2.2 ml) and recorded at DIV8. The samples were then placed in a coupled device camera and preincubated at 37°C in an extracellular solution for 15 min prior to live Ca²⁺ imaging. Then, the samples were mounted on an inverted microscope (Nikon Eclipse Ti-U) and continuously perfused at RT with the same extracellular solution containing the following (in mM): 150 NaCl, 4 KCl, 1 MgCl₂, 2 CaCl₂, 10 HEPES, 10 glucose; pH 7.4. Cells were visualized with a 40× objective (Plan Fluor 0.6 × NA), and recordings were performed from visual fields (680 × 680 μ m², binning 4 × 4). Samples were excited with a mercury lamp at 488 nm. We used a 395 nm dichroic mirror and DN filter (1/32); images were acquired by an ORCA-Flash 4.0 V2 sCMOS camera (Hamamatsu) and a setup controlled by the HCLImage Live software (Hamamatsu). The exposure time ranged from 500 ms to 2 s to prevent bleaching. Live imaging recordings last 30 min for each sample, with movies captured every 10 min.

For ex vivo live Ca²⁺ imaging, AAV-mbp:jGCaMP8s was utilized with the same technical settings employed for in vitro recording. Organotypic spinal cord cultures were infected at DIV7 or DIV14 and recorded after 7 d. The samples were continuously perfused at RT in an extracellular solution with the following composition (in mM): 152 NaCl, 4 KCl, 1 MgCl₂, 2 CaCl₂, 10 HEPES, 10 glucose; pH 7.4. Samples were recorded for a total of 30 min, with movies collected every 10 min. Tetrodotoxin (TTX, HB1035, Hello Bio) was added into the extracellular solution, reaching a final concentration of 1 μ M. Following a 20 min perfusion at RT, samples were recorded for a total of 30 min, with movies collected every 10 min. Additionally, we conducted an ex vivo longitudinal study, recording Ca²⁺ signaling in oligodendrocytes at DIV14, DIV16, and DIV21 within the same field of view. Organotypic spinal cord slices were infected at DIV7 for 7 d. Live imaging recordings in extracellular solution last 20 min for each sample, with movies captured every 10 min. Postrecording at DIV14, half of the medium containing AAV-mbp:jGCaMP8s was replaced with fresh medium, while after the recording at DIV16, 25% of the medium was replaced with a fresh medium. Following the recording at DIV21, the samples were treated for 20 min with PI and fixed. In the context of this study, we define "Ca²⁺ events" as Ca²⁺ waves, specifically referring to events lasting longer than 1 s.

Electrophysiology and calcium imaging of oligodendrocytes. Live Ca²⁺ imaging of oligodendrocytes and single-cell electrophysiology recordings from spinal neurons were simultaneously conducted in the ventral area of DIV14 organotypic cultures before and after TTX (1 μ M) application. Briefly, whole-cell patch-clamp recordings were performed from ventral interneurons visually identified through a microscope (Nikon) on the basis of previously reported criteria (Avossa et al., 2003). During experiments, slices were perfused with extracellular solution as follows (in mM): 152 NaCl, 4 KCl, 1 MgCl₂, 2 CaCl₂, 10 HEPES, 10 glucose, pH 7.4.

Patch pipettes (4–6 M Ω) contained the following (in mM): 120 K gluconate, 20 KCl, 10 HEPES, 10 EGTA, 2 MgCl₂, 2 Na₂ATP. The pH was adjusted to 7.3 with KOH (295 mOsm). All recordings were performed at RT. Data was recorded via the NIS-Elements D 4.66 acquisition software with a 40×/0.80w Nikon Fluor objective. Electrophysiological responses were amplified via MultiClamp 700B (Axon CNS Molecular Devices), with the amplifier's gain set at 1, membrane current 0.5 V/nA, sampled, and digitized at 2 kHz via DigiData 1550B and pCLAMP software (Axon Instruments) for off-line analysis.

In voltage-clamp mode, we considered only recordings where uncompensated series resistance values were <20 M Ω , enabling recordings of synaptic currents without significant distortion. Spontaneous postsynaptic currents were monitored at a holding potential of –56 mV, not compensated for liquid junction potential (–14 mV). Ca²⁺ events (defined as above) were recorded with an exposure time of 150 ms and 2 × 2 binning.

Ca²⁺ live imaging analysis. Recorded movies were analyzed off-line using the Fiji ImageJ and Clampfit (pClamp suite, 10.7 version; Molecular Devices) software. [Ca²⁺]_i waves were expressed as a fractional amplitude increase $\Delta F/F_0$, where F_0 is the baseline fluorescence level and ΔF is the rise over the baseline. F_0 was determined by calculating the average fluorescence intensity during the period of cellular inactivity (for Oregon Green) or as the average of the lowest recorded fluorescence intensity within the same field of view and in the same movie (for AAV-mbp:jGCaMP8s). We defined Ca²⁺ waves as increases in $\Delta F/F_0$ exceeding 20% of the average maximum peak of amplitude recorded in each movie. We

defined the frequency of Ca^{2+} waves as the number of waves observed throughout each recording. We defined as duration the temporal difference between the endpoint and the starting point of the recorded wave; we defined amplitude as the fluorescence intensity at the peak of the detected wave. Data pooled from different cellular regions were integrated to generate a single data point presented as average frequency, average duration, and average amplitude. The collected data were derived from ≥ 5 experiments, each employing a different culture.

RNA extraction and RT-PCR. Total mRNA was isolated from the spinal cord organotypic cultures at DIV14 and DIV21 using a standard TRIzol RNA extraction protocol. The RNA obtained (50 ng) was reverse-transcribed and amplified using Luna Universal Probe One-Step RT-qPCR Kit (New England Biolabs) with sequence-specific primers (1 μM) and probes (200 nM) in a 20 μl reaction, following the manufacturer's instructions. Primers and probes sequences are listed in Table 1. Quantification of *Mbp* gene expression was performed, and the expression of the housekeeping gene *Gapdh* was used for normalization. Amplifications were performed using a Bio-Rad Laboratories CFX96 machine. The real-time qPCR program was executed in accordance with the manufacturer's instructions (annealing 60°C for 30 s).

Polyacrylamide gel electrophoresis (SDS-PAGE) and Western blotting. Spinal cord organotypic culture lysates were prepared in the RIPA buffer (50 mM Tris-HCl, pH 7.5, 150 mM NaCl, 1% (v/v) Nonidet P-40, 0.2% (p/v) sodium deoxycholate) supplemented with a cocktail of protease inhibitors (Roche Diagnostics). For the quantification of the total protein in cellular lysates, the Bradford assay (Bio-Rad Laboratories) was used. All samples were diluted with the Laemmli buffer in the presence of 5% (v/v) β -mercaptoethanol (reduced SDS-PAGE) and heated at 95°C for 5 min. Proteins were resolved by SDS-PAGE and transferred onto a polyvinylidene fluoride membrane (Sigma-Aldrich). Transferred protein bands were visualized by staining with 0.2% (p/v) Ponceau S in 1% (v/v) acetic acid. Subsequently, for MBP (1:1000, Abcam) and MAG (1:1000, D4G3 Cell Signaling Technology) detection, membranes were blocked for 1 h at RT with 5% (p/v) BSA in PBS containing 0.1% Tween 20 (PBS-T). For the detection of *Gapdh* (1:1000, 60004-1-Ig, Proteintech), membranes were blocked with 5% (p/v) nonfat dry milk in PBS. Membranes were then incubated ON at 4°C with the primary antibody diluted in the appropriate blocking solution, washed three times with PBS-T or TBS-T, and incubated for 1 h at RT with the secondary antibody diluted in the blocking solution. Protein bands were visualized using the chemiluminescence detection system (Uvitec). Densitometric analysis of immunoblots was performed using the Fiji ImageJ software.

Statistics. All experiments were performed as independent biological replicates. Statistical analyses and graphs were generated using GraphPad Prism 8.0.1. Testing was performed for normality by the D'Agostino-Pearson omnibus normality test. For normally distributed data, two-tailed unpaired parametric Student's *t* tests were utilized, with equal variance confirmed by the *F* test. Nonnormally distributed data were analyzed using a two-tailed Mann-Whitney test. Pearson's correlation test was used to assess correlation. Throughout all analyses, * $p < 0.05$, ** $p < 0.01$, *** $p < 0.001$, and **** $p < 0.0001$. Detailed statistical methods for each figure are provided in an attached table of statistics (Table 2). The number of cultures analyzed for each experiment and each condition was ≥ 3 , unless otherwise stated.

Results

We engineered a rAAV to deliver the newly released GECI transgene, specifically jGCaMP8s, under the transcriptional control of the MBP promoter to drive its expression specifically in myelinating oligodendrocytes. Purified viral particles were used to infect both primary rat oligodendrocyte cultures and mouse organotypic spinal cord slices (Fig. 1).

AAV-mbp;jGCaMP8s expression in oligodendrocytes in vitro

It is well established that primary cultures of OPCs, in the absence of neurons, are capable of differentiating and synthesizing MBP, a protein produced solely by mature oligodendrocytes (Friess et al., 2016). Oligodendrocyte cultures were infected with AAV-mbp;jGCaMP8s and maintained in culture for 4 d prior to live Ca^{2+} imaging at DIV8. We detected eGFP expression in $>70\%$ of MBP⁺ oligodendrocytes (Fig. 2A; Extended Data Fig. 2-1). Our cultures, primarily consisting of enriched OPCs populations, were derived from mixed glial cultures; therefore, to assess the specificity of our construct, we excluded the expression of AAV-mbp;jGCaMP8s in glial fibrillary acidic protein (GFAP)⁺ astrocytes. As illustrated in Figure 2B, eGFP⁺ cells exhibit no colocalization with GFAP⁺ cells.

By live imaging, we recorded spontaneous Ca^{2+} episodes localized in myelinating processes (Fig. 2C, arrows, D; Movies 1 and 2), consistently with prior reports (Rui et al., 2020). $[\text{Ca}^{2+}]_i$ events exhibited substantial heterogeneity in frequency, duration, and amplitude values among oligodendrocyte processes (Fig. 2E-G). A positive correlation between duration and amplitude of Ca^{2+} events was observed, namely, longer oscillations displayed at higher amplitudes (Fig. 2H).

We compared the efficiency of AAV-mbp;jGCaMP8s and Oregon Green 488 BAPTA-1 AM, a commonly used Ca^{2+} imaging dye, to measure $[\text{Ca}^{2+}]_i$ signaling. In oligodendrocytes cultures, Ca^{2+} events detected by AAV-mbp;jGCaMP8s displayed comparable dynamic features as those detected by Oregon Green, using the same acquisition time frame and exposure time (>1 s), but the rAAV strategy improved the oligodendrocyte processes spatial resolution (compare Fig. 2C,I,J; Movies 1 and 2). Overall, these results demonstrate the efficacy and specificity of the developed rAAV, allowing detection of Ca^{2+} signals even from microdomains within the cell processes, thereby providing an experimental improvement in monitoring Ca^{2+} dynamics in myelinating oligodendrocytes.

Table 2. Summary statistics

Figure	Parameter	Type of test	Sample size	Statistical data
Figure 2H	Correlation amplitude versus duration of Ca ²⁺ events	Pearson's correlation <i>t</i> test, two-tailed	<i>N</i> = 315 oligodendrocyte processes	<i>r</i> = 0.67 <i>p</i> < 0.0001
Figure 2J	Frequency, duration and amplitude of Ca ²⁺ events	Unpaired parametric <i>t</i> test, two-tailed	<i>N</i> = 10 (jGCaMP8s), <i>N</i> = 15 (Oregon Green) movies	F: <i>t</i> = 0.8814; df = 23; <i>p</i> = 0.386 D: <i>t</i> = 0.3840; df = 27; <i>p</i> = 0.704 A: <i>t</i> = 0.6385; df = 29; <i>p</i> = 0.528
Figure 3E	Efficiency (%)		<i>N</i> = 3 (eGFP), <i>N</i> = 3 (eGFP/MBP)	eGFP (mean ± SEM): 89.29 ± 8 eGFP/MBP (mean ± SEM): 74.91 ± 5.9
Figure 3I	Average frequency of Ca ²⁺ events	Unpaired parametric <i>t</i> test, two-tailed	220 (control), 135 (TTX) oligodendrocyte processes; <i>N</i> = 16 (control), <i>N</i> = 10 (TTX) movies	<i>t</i> = 0.3554; df = 24; <i>p</i> = 0.7254
Figure 3J	Average duration of Ca ²⁺ events	Unpaired <i>t</i> test Two-tailed Mann-Whitney	220 (control), 135 (TTX) oligodendrocyte processes; <i>N</i> = 16 (control), <i>N</i> = 10 (TTX) movies	<i>p</i> = 0.0328
Figure 3K	Average amplitude of Ca ²⁺ events	Unpaired <i>t</i> test Two-tailed Mann-Whitney	220 (control), 135 (TTX) oligodendrocyte processes; <i>N</i> = 16 (control), <i>N</i> = 10 (TTX) movies	<i>p</i> < 0.0001
Figure 4C	Average frequency of Ca ²⁺ events	Unpaired <i>t</i> test Two-tailed Mann-Whitney	183 (control), 49 (TTX) oligodendrocyte processes; <i>N</i> = 13 (control), <i>N</i> = 5 (TTX) movies	<i>t</i> = 0.3735; df = 16; <i>p</i> = 0.9241
Figure 4D	Average duration of Ca ²⁺ events	Unpaired <i>t</i> test Two-tailed Mann-Whitney	183 (control), 49 (TTX) oligodendrocyte processes; <i>N</i> = 13 (control), <i>N</i> = 5 (TTX) movies	<i>p</i> = 0.2751
Figure 4E	Average amplitude of Ca ²⁺ events	Unpaired <i>t</i> test Two-tailed Mann-Whitney	183 (control), 49 (TTX) oligodendrocyte processes; <i>N</i> = 13 (control), <i>N</i> = 5 (TTX) movies	<i>p</i> = 0.3140
Figure 4G	Correlation amplitude vs duration of Ca ²⁺ events	Pearson's correlation Two-tailed	<i>N</i> = 183 (control), <i>N</i> = 49 (TTX) oligodendrocyte processes	<i>r</i> = 0.46, <i>p</i> < 0.0001 (control); <i>r</i> = 0.22, <i>p</i> = 0.005 (TTX)
Figure 4H	Average frequency of Ca ²⁺ events	Unpaired parametric <i>t</i> test, Two-tailed	220 (DIV14), 183 (DIV21) oligodendrocyte processes; <i>N</i> = 16 (control), <i>N</i> = 13 (TTX) movies	<i>t</i> = 1.089; df = 27; <i>p</i> = 0.2857
Figure 4I	Average duration of Ca ²⁺ events	Unpaired <i>t</i> test Two-tailed Mann-Whitney	220 (DIV14), 183 (DIV21) oligodendrocyte processes; <i>N</i> = 16 (control), <i>N</i> = 13 (TTX) movies	<i>p</i> < 0.0001
Figure 4J	Average amplitude of Ca ²⁺ events	Unpaired <i>t</i> test Two-tailed Mann-Whitney	220 (DIV14), 183 (DIV21) oligodendrocyte processes; <i>N</i> = 16 (control), <i>N</i> = 13 (TTX) movies	<i>p</i> < 0.0001
Figure 4L	Number of branches per OL	Unpaired parametric <i>t</i> test Two-tailed	11 (DIV14), 11 (DIV21) oligodendrocyte processes; <i>N</i> = 3 (DIV14), <i>N</i> = 3 (DIV21) movies	<i>t</i> = 2.371; df = 20, <i>p</i> = 0.0279
Figure 4M	Sheath length	Unpaired parametric <i>t</i> test Two-tailed	11 (DIV14), 11 (DIV21) oligodendrocyte processes; <i>N</i> = 3 (DIV14), <i>N</i> = 3 (DIV21) movies	<i>t</i> = 0.1436; df = 18, <i>p</i> = 0.8874
Figure 4N	Total myelin sheath per OL	Unpaired <i>t</i> test Two-tailed Mann-Whitney	11 (DIV14), 11 (DIV21) oligodendrocyte processes; <i>N</i> = 3 (DIV14), <i>N</i> = 3 (DIV21) movies	<i>p</i> = 0.0433
Figure 4O	MBP and MAG protein expression	Unpaired parametric <i>t</i> test Two-tailed	<i>N</i> = 3 (DIV14), <i>N</i> = 3 (DIV21) spinal cord organotypic cultures	MBP: <i>t</i> = 3.379; df = 4, <i>p</i> = 0.0278 MAG: <i>t</i> = 3.682; df = 4, <i>p</i> = 0.0212
Figure 4P	MBP RNA expression	Unpaired <i>t</i> test Two-tailed Mann-Whitney	<i>N</i> = 5 (DIV14), <i>N</i> = 5 (DIV21) spinal cord organotypic cultures	<i>p</i> = 0.0317

Bold values are statistically significant, which means *p* < 0.05.

Figure 2H: *****p* < 0.0001; Figure 3J: **p* = 0.0328; Figure 3K: *****p* < 0.0001; Figure 4G: *****p* < 0.0001, ***p* = 0.005; Figure 4I: *****p* < 0.0001; Figure 4J: *****p* < 0.0001; Figure 4L: **p* = 0.0279; Figure 4N: **p* = 0.0433; Figure 4O: **p* = 0.0278, **p* = 0.0212; Figure 4P: **p* = 0.0317.

Step 1: Production of AAVs (transfection, harvest, purification, and titration).

Step 2: Evaluation of transgene expression.

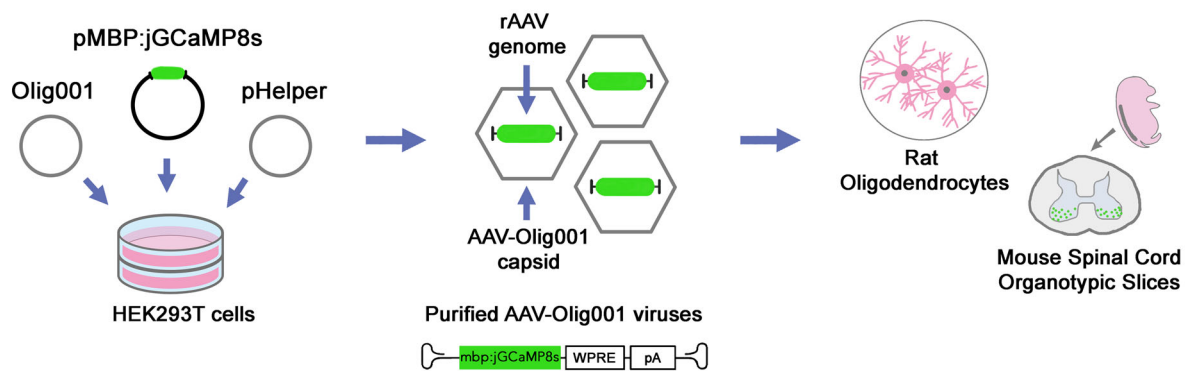


Figure 1. Protocol overview. The procedure consists of two main steps: AAV production and evaluation of transgene expression through Ca^{2+} imaging analysis in primary oligodendrocyte and in organotypic spinal cord cultures. The AAV-mbp:jGCaMP8s is obtained through a triple-plasmid transfection process using HEK293T cells, including the cloned vector containing a green fluorescent reporter (jGCaMP8s), the Rep/Cap plasmid Olig001, and the helper plasmid (Step 1). After collection, purification, and titration, AAV-mbp:jGCaMP8s viral particles were administered to primary oligodendrocyte cultures or organotypic spinal cord slices (Step 2).

Ca^{2+} dynamics in oligodendrocytes during spinal slice culture development

We exploited AAV-mbp:jGCaMP8s specificity in organotypic spinal cord cultures, where sensory, motor, and interneuron circuit development are accompanied by resident glia cell progressive maturation (Avossa et al., 2003). Spinal slices were administered with AAV-mbp:jGCaMP8s at DIV7 and imaged at DIV14. Immunostaining with MBP antibody confirmed that the rAAV expression was specific to myelinating oligodendrocytes; accordingly, eGFP⁺ cells exhibited the unique oligodendrocyte localization and morphology (Fig. 3A,B), while neurons, marked by SMI-32, a neurofilament marker, were not eGFP⁺ (Fig. 3C). This becomes notably clearer when examining confocal images at higher magnification of SMI-32⁺ axons ensheathed by eGFP⁺ and MBP⁺ processes (Fig. 3D; Extended Data Fig. 3-1). Quantification of MBP⁺/eGFP⁺ cells further supported the specificity of rAAV expression in myelinating oligodendrocytes (Fig. 3E), without significantly affecting cell death (Extended Data Fig. 3-2). Staining with GFAP and Iba1, targeting astrocytes and microglia, respectively, confirmed the absence of colocalization with eGFP⁺ cells (Fig. 3F,G). Collectively, this data indicates that AAV-mbp:jGCaMP8s in spinal cultures selectively targets myelinating oligodendrocytes while excluding neurons and other resident glial cell types.

Based on these findings, we performed live Ca^{2+} imaging in spinal cord tissues at DIV14, detecting Ca^{2+} events localized in oligodendrocytes processes (Fig. 3H,L) and measuring the average values of frequency, duration, and amplitude (Fig. 3I-K; Movies 3 and 4). Since neuronal activity might modulate $[\text{Ca}^{2+}]_i$ signaling in oligodendrocytes (Pitman and Young, 2016), we selectively blocked fast voltage-gated Na^+ channels by applying TTX (1 μM) to the spinal cultures (Panattoni et al., 2021). TTX treatment roughly halved the Ca^{2+} events amplitude in oligodendrocytes processes while significantly decreasing their duration without affecting the average Ca^{2+} frequency (Fig. 3I-L; Movies 3 and 4). Simultaneous recording of oligodendrocytes Ca^{2+} signaling and electrophysiology in neurons allowed us to further confirm these findings (Extended Data Fig. 3-3). In both the control and TTX-treated slices, we did not observe a significant correlation between Ca^{2+} amplitude and duration (Extended Data Fig. 3-4).

During differentiation, oligodendrocytes might undergo profound changes in cellular interactions, neurotransmitter receptor expression, and their overall response to neuronal activity (Clemente et al., 2013; Moura et al., 2022). We tracked Ca^{2+} activity at a later stage of development, namely, at DIV21 to explore whether distinct Ca^{2+} signals are generated by oligodendrocytes during spinal circuit maturation (Fig. 4A; Rosato-Siri et al., 2004). Immunohistochemical analysis showed that >80% of the eGFP⁺ cells colabeled with MBP, while no colocalization was detected with neurons and other glial cells (Extended Data Fig. 4-1). We investigated the effect of neuronal activity on oligodendrocyte Ca^{2+} dynamics in spinal cord cultures at DIV21 (Fig. 4B-F). Our analysis showed no significant alterations in the average frequency, duration, and amplitude of Ca^{2+} events when neuronal action potentials were inhibited by TTX (Fig. 4C-F; Movies 5 and 6). Differently from DIV14, we observed a significant positive correlation between amplitude and duration of Ca^{2+} signals in both the control and TTX conditions (Fig. 4G).

Besides the changes in the amplitude/duration correlation and in TTX sensitivity over the period of oligodendrocyte in vitro maturation and myelin stabilization around axons, we directly compared the average values of frequency, amplitude, and duration of Ca^{2+} signals in the spinal cultures between DIV14 and DIV21. We observed a remarkable decline in both amplitude and duration of Ca^{2+} events as development progressed (Fig. 4I,J), while the frequency remained unaffected (Fig. 4H). Longitudinal live imaging highlighted dynamic changes in Ca^{2+} duration and amplitude of oligodendrocytes throughout development without affecting long-term viability (Fig. 4K; Extended Data Fig. 4-2), along with increased

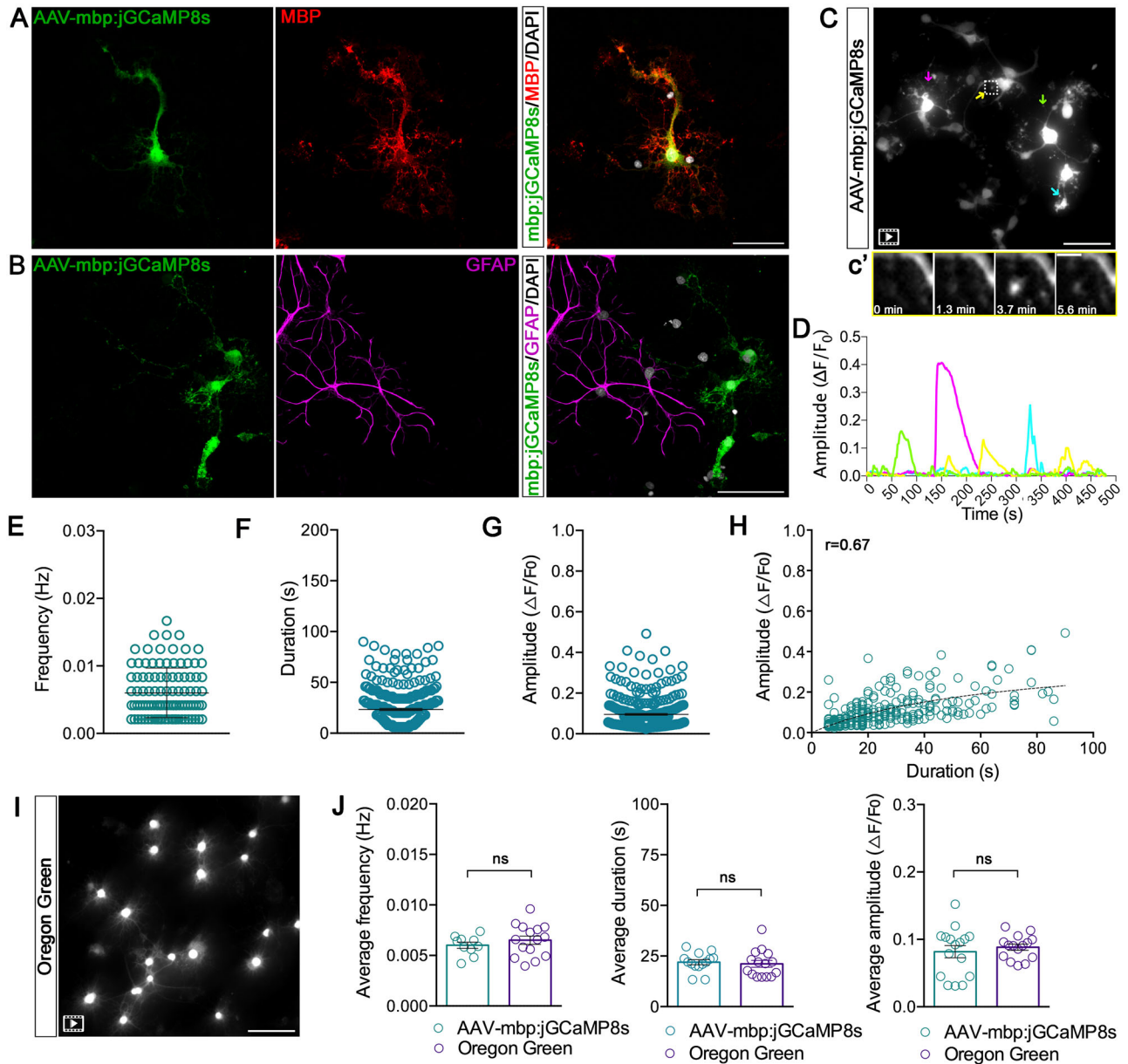
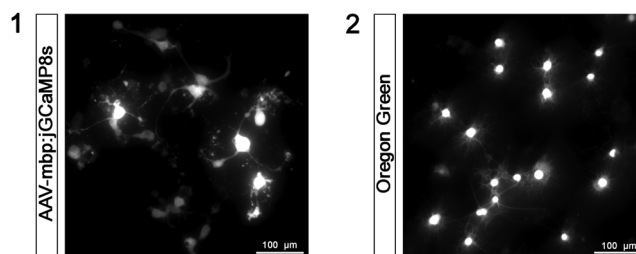
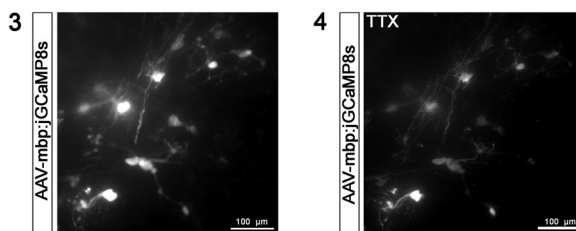


Figure 2. Live imaging reveals Ca^{2+} activity in primary oligodendrocyte cultures using AAV-mbp:jGCaMP8s. **A**, Representative confocal micrograph of myelinating oligodendrocytes (DIV8) showing eGFP expression for jGCaMP8s (green) and mature oligodendrocytes (MBP, red). Nuclei (white) were labeled with DAPI dye. Scale bar, 100 μm . See Extended Data Figure 2-1 for more details. **B**, Representative confocal micrograph of myelinating oligodendrocytes showing eGFP expression for jGCaMP8s (green) and of GFAP⁺ astrocytes (magenta). Nuclei (white) were labeled with DAPI dye. Scale bar, 100 μm . **C**, Maximum intensity projection of a 3D z-stack, illustrating an extended-duration movie highlighting jGCaMP8s-expressing myelinating oligodendrocytes. Arrowheads indicate oligodendrocyte processes shown in corresponding colors in fluorescent traces in **D**. Scale bar, 100 μm . Frames from the time-lapse imaging are indicated with a white box corresponding to panel **c'** (Movies 1 and 2). Scale bar, 10 μm . **D**, Representative traces of $\Delta F/F_0$ over time. **E**, Distribution of Ca^{2+} events frequencies (Hz) per oligodendrocyte process. **F**, Distribution of Ca^{2+} events duration per oligodendrocyte process. **G**, Distribution of Ca^{2+} events amplitude per oligodendrocyte process. **H**, Correlation between amplitude and duration per individual Ca^{2+} events (Pearson's correlation test, $r=0.67$; $p<0.0001$). **I**, Maximum intensity projection of a 3D z-stack, illustrating an extended-duration movie highlighting Oregon Green 488 BAPTA-1-expressing myelinating oligodendrocytes (Movies 1 and 2). Scale bar, 100 μm . **J**, Distribution of average frequency, duration, and amplitude of Ca^{2+} events per oligodendrocyte process. Comparison between AAV-mbp:jGCaMP8s and Oregon Green 488 BAPTA-1 AM indicator. A two-tailed statistical unpaired t test was used from 315 (AAV-mbp:jGCaMP8s) and 217 (Oregon Green) oligodendrocyte processes, analyzed from $N=10$ (AAV-mbp:jGCaMP8s) and $N=15$ (Oregon Green) movies. **** $p\leq 0.0001$; ns, not significant.

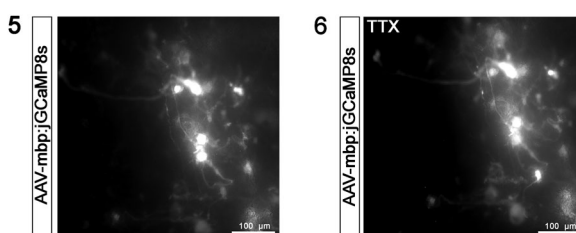
oligodendrocyte branching complexity at DIV21 (Fig. 4L; Movies 7–9). Although sheath length remained consistent (Fig. 4M), the greater sheath number at DIV21 resulted in a higher total amount of myelin per oligodendrocyte (Fig. 4N). Accordingly, expression levels of MBP and MAG proteins were higher at DIV21 compared with those at DIV14 (Fig. 4O), accompanied by elevated *Mbp* RNA expression (Fig. 4P). These findings suggest an enhanced myelinating



Movies 1 and 2. Myelin Ca^{2+} events in primary oligodendrocyte cultures infected with AAV-mbp;jCaMP8s (1) [view online] and administered with Oregon Green 488 BAPTA-1 A.M. (2) [view online], related to Figure 2C and Figure 2I, respectively.



Movies 3 and 4. Myelin Ca^{2+} events in an organotypic spinal cord culture at DIV14 infected with AAV-mbp;jCaMP8s (3) [view online] and treated with TTX (4) [view online], related to Figure 3H.



Movies 5 and 6. Myelin Ca^{2+} events in an organotypic spinal cord culture at DIV21 infected with AAV-mbp;jCaMP8s (5) [view online] and treated with TTX (6) [view online], related to Figure 4B.

capacity per oligodendrocyte during the development of organotypic spinal cord cultures. Overall, our results suggest a developmental regulation of $[\text{Ca}^{2+}]_i$ dynamics in oligodendrocytes with a transient dependence upon action potential firing.

Discussion

Our major result is the successful characterization of a recombinant viral vector expressing the jCaMP8s under the control of the MBP promoter. We exploited AAV-mbp;jCaMP8s to visualize and monitor Ca^{2+} activity in myelinating oligodendrocytes in vitro and in ex vivo slice cultures. This model sheds light on the expression of MBP, a critical myelin protein (Chernoff, 1981), in concert with fluctuations in $[\text{Ca}^{2+}]_i$ during myelination. jCaMP8s expression was histologically and functionally shown to be restricted to mature oligodendrocytes in both models, such a selectivity was particularly evident in spinal cord organotypic cultures, where numerous resident glial cells are present and eGFP⁺ oligodendrocytes tightly ensheath SMI32⁺ axons.

In recent studies, myelin Ca^{2+} activity was investigated in transgenic zebrafish and rodent animal models (Krasnow et al., 2018; Battefeld et al., 2019). While rAAVs are an easier and cost-effective approach, their utility is limited by the lack of natural AAV capsids with oligodendrocyte affinity. Our study successfully exploited the viral capsid Olig001 which displayed exceptional in vivo tropism for oligodendrocytes (Powell et al., 2016). The specificity of AAV-mbp;jCaMP8s in myelinating oligodendrocytes was further reinforced by the absence of colocalization with microglia and neurons in organotypic cultures, as well as with astrocytes in both cultured models.

Comparing its kinetics to Oregon Green BAPTA-1, the current AAV-mbp;jCaMP8s displayed a similar response, due to our imaging settings (Sun et al., 2013). However, the chemical probe showed a lower spatial resolution required for optimal measuring of Ca^{2+} signals in oligodendrocytes processes. The robust expression of AAV-mbp;jCaMP8s in mature

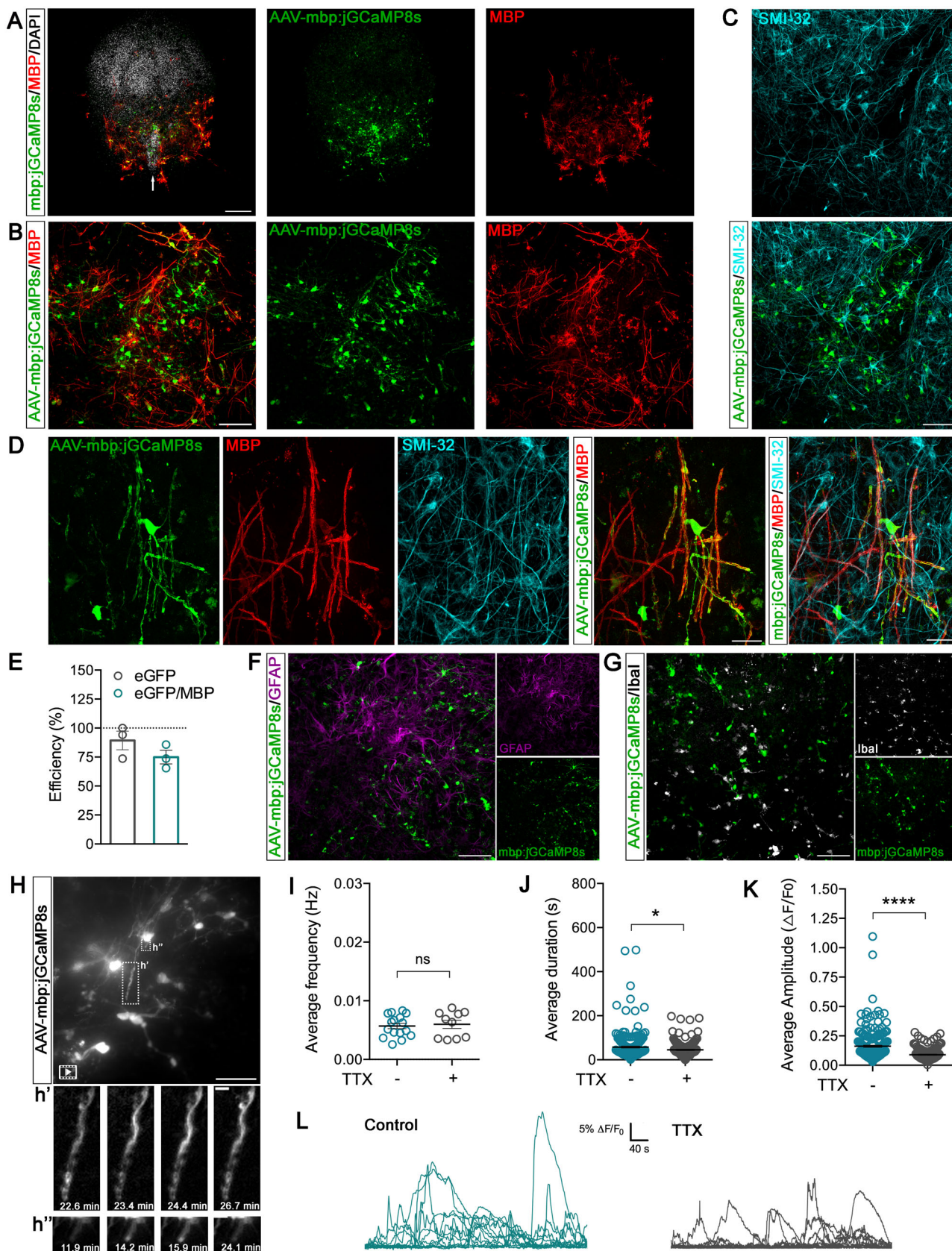


Figure 3. Continued.

oligodendrocytes not only enabled precise imaging of Ca^{2+} events in myelin processes but also demonstrated its suitability for chronic and high-resolution Ca^{2+} signaling recordings without affecting total cell death. One methodological consideration is the sampling rate (~ 0.03 Hz) employed for detecting Ca^{2+} events, determined by our imaging setup. This design limited our observations to Ca^{2+} events longer than the subsecond duration Ca^{2+} transients.

We focused on the development of our versatile tool to record the spatiotemporal pattern of Ca^{2+} changes in myelinating spinal organ cultures. We observed a substantial number of traced axons ensheathed by MBP protein, together with a highly active period of spontaneous Ca^{2+} events during the early postnatal week. At this age, individual oligodendrocytes make short myelin sheaths on multiple axons, retracting from some axons while maintaining sheaths on others (Czopka et al., 2013); this dynamic process is directly correlated with Ca^{2+} signals as demonstrated by Baraban et al. (2018). Up to now, Ca^{2+} changes in OPCs processes have largely been suggested as dependent on neuronal action potentials (Wake et al., 2011). Unexpectedly, our results indicated that the Ca^{2+} frequency was independent of action potential generation both at DIV14 and DIV21. Conversely, only at DIV14, Ca^{2+} amplitude and duration significantly decreased following the pharmacological blockade of neuronal activity, whereas no significant modulation was observed at DIV21. These data suggest that Ca^{2+} events in oligodendrocytes can be sustained by both neuronal activity and intrinsic mechanisms (Hamilton et al., 2017; Rui et al., 2020; Fiore et al., 2022). In particular, myelination regulates the influx of extracellular Ca^{2+} and its uptake from endoplasmic reticulum and mitochondria depending on the developmental stage (Krasnow et al., 2018; Paez and Lyons, 2020; Meyer and Rinholm, 2021). The morphology, density, and spatial distribution of mitochondria reflect the modulation of energy demand and Ca^{2+} buffering capacity in oligodendrocytes during development. Mature oligodendrocytes are sustained by glycolysis and characterized by smaller and fewer mitochondria. In contrast, OPCs and developing oligodendrocytes have a higher metabolic demand, exhibiting a dense population of elongated mitochondria. These cells use both glycolysis and oxidative phosphorylation to produce energy for lipid biosynthesis and active myelination (Kirischuk et al., 1995; Rinholm et al., 2016; Rone et al., 2016; Meyer and Rinholm, 2021; Narine and Colognato, 2022). Our results showed a stage-dependent decline in the Ca^{2+} amplitude and duration during myelination. Specifically, spinal slices at DIV14 display heightened amplitude and prolonged duration compared with those at DIV21, without alterations in the frequency of Ca^{2+} events. Interestingly, large-amplitude of Ca^{2+} waves occurred primarily between DIV13 and DIV15 in brain slices, coinciding with a phase of rapid longitudinal remodeling of myelin (Battfeld et al., 2019).

Our results suggest a decreased energy demand from oligodendrocytes with age, indicating possible modifications in mitochondrial morphology, density, and Ca^{2+} buffering capacity, all issues needing further investigations. Interestingly, the absence of correlation between Ca^{2+} events amplitude and duration at DIV14 in spinal organ slices, observed in both the control and TTX conditions, could be attributed to the fact that among MBP-expressing cells some are wrapping axons, while others are maintaining myelin. These simultaneous activities reveal a heterogeneous energy demand and Ca^{2+} buffering capacity among oligodendrocytes, accompanied by a combined glycolysis-OXPHOS ATP production. In this phase, neuronal activity partially contributes to Ca^{2+} buffering capacity, underscoring that myelination may also be regulated by additional Ca^{2+} -mediated pathways. However, at DIV21, the correlation between Ca^{2+} amplitude and duration was recovered, potentially due to the majority of axons being already myelinated and oligodendrocytes being mainly involved in maintaining myelin sheaths with a low ATP production through the glycolytic pathway. This reliance on glycolysis could result in a similar Ca^{2+} buffering capacity among mitochondria. Thus, Ca^{2+} dynamics in organ cultures between DIV14 and DIV21 align with significant morphological changes in oligodendrocytes, evidenced by enhanced myelin production per oligodendrocyte, increased number of branches, elevated expression of MBP and MAG proteins, and augmented levels

Figure 3. Ex vivo AAV-mbp:jGCaMP8s screening in spinal cord organ cultures at DIV14. **A**, Representative image of the whole spinal organotypic culture showing AAV-mbp:jGCaMP8s expression (green) and mature oligodendrocytes (MBP, red). Nuclei (white) were labeled with DAPI dye. Note the ventral region highlighted by the ventral fissure (arrow). Scale bar, 300 μm . **B**, Representative higher magnification image of the spinal ventral region (same as in **A**) showing AAV-mbp:jGCaMP8s expression (green) and mature oligodendrocytes (MBP, red). Scale bar, 100 μm . See Extended Data Figure 3-1 for more details. **C**, Representative confocal micrograph of spinal organotypic ventral region showing neurons (SMI-32, cyan) and AAV-mbp:jGCaMP8s expression (green). Scale bar, 100 μm . **D**, Representative higher magnification images of spinal cord organotypic cultures showing AAV-mbp:jGCaMP8s expression (green), mature oligodendrocytes (MBP, red), and neurons (SMI-32, cyan). Scale bar, 30 μm . **E**, Quantification of the AAV-mbp:jGCaMP8s efficiency in spinal cord organotypic cultures at DIV14. Data are represented as percentages. The analysis was performed using maximum intensity projections of 3D z-stack images, and quantification was obtained by using the “Analyze particles” function of the Fiji ImageJ software; $N = 3$ spinal cord organotypic cultures. **F**, Representative image of ventral region of spinal cord organotypic cultures showing AAV-mbp:jGCaMP8s expression (green) and GFAP⁺ astrocytes (magenta). Scale bar, 100 μm . **G**, Representative image of ventral region (same as in **F**) showing AAV-mbp:jGCaMP8s expression (green) and microglia (Ibal, white). Scale bar: 100 μm . **H**, Maximum intensity projection of a 3D z-stack, illustrating an extended-duration movie highlighting jGCaMP8s-expressing myelinating oligodendrocytes. Scale bar, 100 μm . Frames from the time-lapse imaging are indicated with a white box corresponding to panel **h'**, **h''**; scale bar, 10 μm . **I**, Average distribution of Ca^{2+} wave frequencies (Hz) per oligodendrocyte process before and after application of TTX. **J**, Average distribution of Ca^{2+} wave duration per oligodendrocyte process before and after application of TTX. **K**, Average distribution of Ca^{2+} amplitude per oligodendrocyte process before and after application of TTX. **L**, Representative traces of $\Delta F / F_0$ over time before and after application of TTX. Scale bar, 40 s, and 5% $\Delta F / F_0$. Two hundred twenty (control) and one hundred thirty-five (TTX) oligodendrocyte processes, analyzed from $N = 16$ (control) and $N = 10$ (TTX) movies. Two-tailed statistical tests used: unpaired parametric t test in **I** and Mann-Whitney in **J** and **K**. * $p < 0.05$; *** $p \leq 0.001$; ns, not significant. See Extended Data Figures 3-2–3-4 and Movies 3 and 4 for more details.

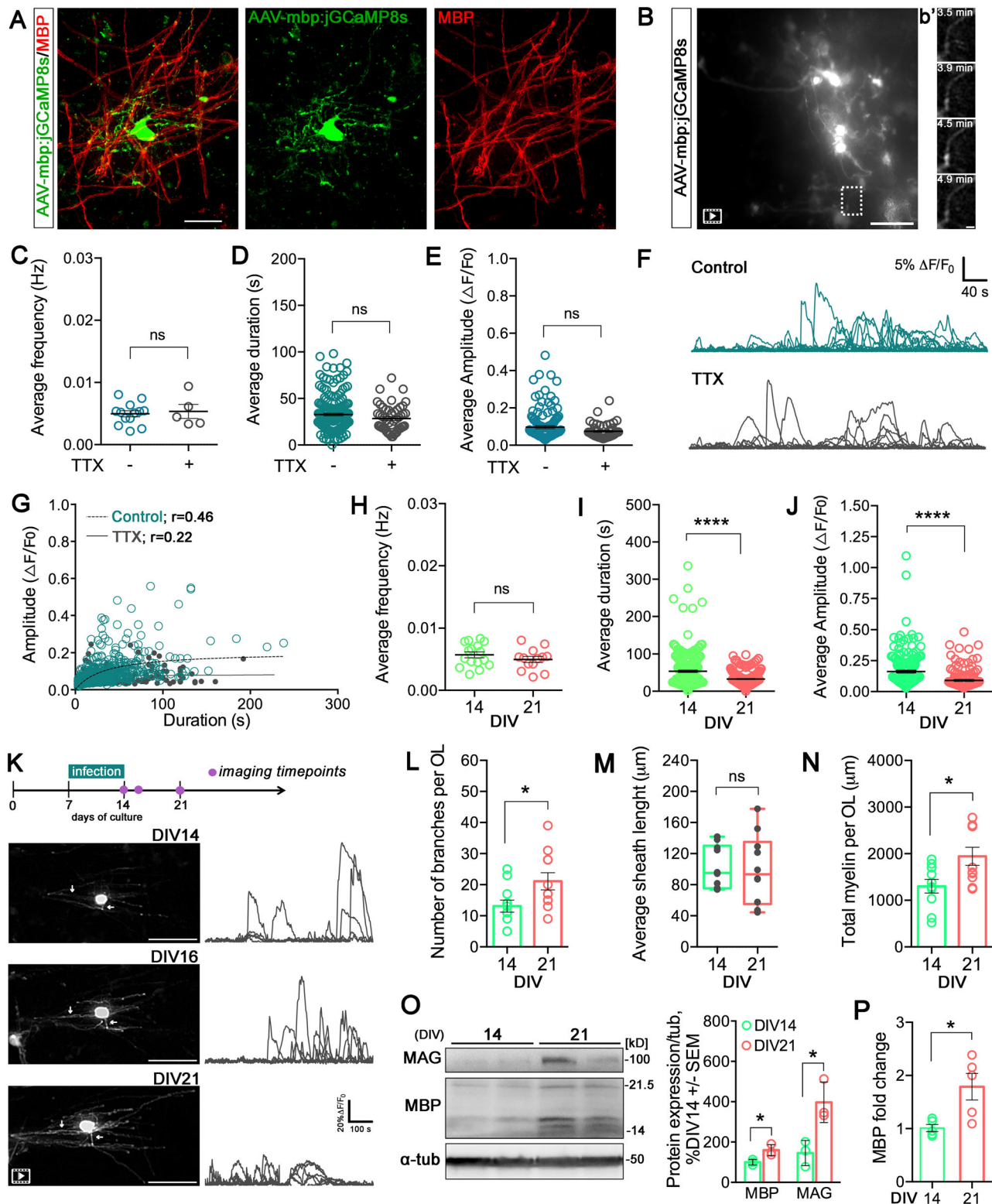
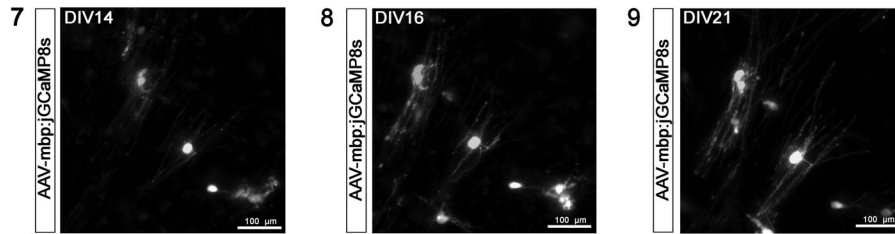


Figure 4. Ex vivo AAV-mbp:jGCaMP8s screening in spinal cord organ cultures at DIV21. **A**, Representative image of the ventral region of spinal cord showing AAV-mbp:jGCaMP8s expression (green) and mature oligodendrocytes (MBP, red). Scale bar, 30 μm . See Extended Data Figure 4-1 for more details. **B**, Maximum intensity projection of a 3D z-stack, illustrating an extended-duration movie highlighting jGCaMP8s-expressing myelinating oligodendrocytes. Scale bar, 100 μm . Frames from the time-lapse imaging are indicated with a white box corresponding to panel **b'**; scale bar, 10 μm . **C**, Distribution of average Ca^{2+} wave frequencies (Hz) of 183 (control) and 49 (TTX) oligodendrocyte processes, analyzed from $N=13$ (control) and $N=5$ (TTX) movies. A two-sided statistical unpaired parametric t test was used; ns, not significant. **D**, Distribution of average Ca^{2+} wave duration of 183 (control) and 49 (TTX) oligodendrocyte processes, analyzed from $N=13$ (control) and $N=5$ (TTX) movies. A two-tailed statistical Mann-Whitney test was used; ns, not significant.



Movies 7, 8 and 9. Ca^{2+} imaging for the ex vivo longitudinal study tracking myelinating oligodendrocytes at DIV14 (**7**) [view online], DIV16 (**8**) [view online], and DIV21 (**9**) [view online], related to [Figure 4K](#).

of MBP mRNA expression levels as development progresses. Taken together, our study provides new evidence regarding the role of Ca^{2+} signaling in mediating different stages of myelination.

Ca^{2+} cellular sources and signaling pathways in mature oligodendrocytes remain poorly understood ([Thornton and Hughes, 2020](#)) and need further explorations. Nonetheless, the employment of AAV-mbp;GCaMP8s with high-resolution Ca^{2+} imaging, coupled with the manipulation of neuronal activity, not only enhances the spatiotemporal resolution of the recordings but also holds the potential to accelerate our understanding of how Ca^{2+} intrinsically regulates oligodendrocyte myelination.

References

- Allen NJ, Lyons DA (2018) Glia as architects of central nervous system formation and function. *Science* 362:181–185.
- Avossa D, Rosato-Siri MD, Mazzarol F, Ballerini L (2003) Spinal circuits formation: a study of developmentally regulated markers in organotypic cultures of embryonic mouse spinal cord. *Neuroscience* 122:391–405.
- Baraban M, Koudelka S, Lyons DA (2018) Ca^{2+} activity signatures of myelin sheath formation and growth in vivo. *Nat Neurosci* 21:19–23.
- Battefeld A, Popovic MA, de Vries SI, Kole MHP (2019) High-frequency microdomain Ca^{2+} transients and waves during early myelin internode remodeling. *Cell Rep* 26:182–191.e5.
- Chakrabarti S, Pattison LA, Doleschall B, Rickman RH, Blake H, Callejo G, Heppenstall PA, Smith ESJ (2020) Intraarticular adeno-associated virus serotype AAV-PHP.S-mediated chemo-genetic targeting of knee-innervating dorsal root ganglion neurons alleviates inflammatory pain in mice. *Arthritis Rheumatol* 72:1749–1758.
- Chen D, Huang Y, Shi Z, Li J, Zhang Y, Wang K, Smith AD, Gong Y, Gao Y (2020) Demyelinating processes in aging and stroke in the central nervous system and the prospect of treatment strategy. *CNS Neurosci Ther* 26:1219–1229.
- Chernoff GF (1981) Shiverer: an autosomal recessive mutant mouse with myelin deficiency. *J Hered* 72:128.
- Clemente D, Ortega MC, Melero-Jerez C, de Castro F (2013) The effect of glia-glia interactions on oligodendrocyte precursor cell biology during development and in demyelinating diseases. *Front Cell Neurosci* 7:268.
- Czopka T, Ffrench-Constant C, Lyons DA (2013) Individual oligodendrocytes have only a few hours in which to generate new myelin sheaths in vivo. *Dev cell* 25:599–609.
- Dai J, Mercury KK, Macklin WB (2014) Interaction of mTOR and Erk1/2 signaling to regulate oligodendrocyte differentiation. *Glia* 62:2096–2109.
- Fiore F, Dereddi RR, Alhalaseh K, Coban I, Harb A, Agarwal A (2022) Norepinephrine regulates Ca^{2+} signals and fate of oligodendrocyte progenitor cells in the cortex, [bioRxiv 2022.08.31.505555](#).
- Friess M, Hammann J, Unichenko P, Luhmann HJ, White R, Kirischuk S (2016) Intracellular ion signaling influences myelin basic protein

E, Distribution of average Ca^{2+} amplitude of 183 (control) and 49 (TTX) oligodendrocyte processes, analyzed from $N = 13$ (control) and $N = 5$ (TTX) movies. A two-tailed statistical Mann–Whitney test was used; ns, not significant. **F**, Representative traces of $\Delta F/F_0$ over time before and after application of TTX. Scale bar, 40 s, and 5% $\Delta F/F_0$. **G**, Correlation between amplitude and duration of individual Ca^{2+} events of 183 (control) and 49 (TTX) oligodendrocyte processes, analyzed from $N = 13$ (control) and $N = 5$ (TTX) movies [Pearson’s correlation, $r = 0.46$; $p < 0.0001$ (control); $r = 0.22$; $p = 0.005$ (TTX); [Movies 5, 6](#)]. **H**, Distribution of average Ca^{2+} events frequencies (Hz) between 220 (DIV14) and 183 (DIV21) oligodendrocyte processes, analyzed from $N = 16$ (DIV14) and $N = 13$ (DIV21) movies. A two-tailed statistical unpaired parametric t test was used; ns, not significant. **I**, Distribution of average Ca^{2+} events duration between 220 (DIV14) and 183 (DIV21) oligodendrocyte processes, analyzed from $N = 16$ (DIV14) and $N = 13$ (DIV21) movies. A two-tailed statistical Mann–Whitney test was used; $***p < 0.0001$. **J**, Distribution of average Ca^{2+} events amplitude between 220 (DIV14) and 183 (DIV21) oligodendrocyte processes, analyzed from $N = 16$ (DIV14) and $N = 13$ (DIV21) movies. A two-tailed statistical Mann–Whitney test was used; $***p < 0.0001$. **K**, Experimental timeline of Ca^{2+} imaging for the ex vivo longitudinal study tracking myelinating oligodendrocytes at DIV14, DIV16, and DIV21. White arrows indicate sheaths that became longer, over 7 d. In the right panel, oligodendrocyte Ca^{2+} traces for three developmental stages showing traces recorded sequentially in different single-cell processes ([Movies 7–9](#)). Scale bar, 100 s, and 20% $\Delta F/F_0$. Experiments were independently repeated three times. See Extended Data [Figure 4–2](#) for more details. **L**, Quantification of the number of branches at DIV14 and DIV21. Points represent individual oligodendrocytes. A two-tailed statistical unpaired t test was used; $*p \leq 0.05$. **M**, Quantification of myelin sheaths length at DIV14 and DIV21. Points represent the average of myelin sheaths of individual oligodendrocytes. A two-tailed statistical unpaired t test was used; ns, not significant. **N**, Quantification of total myelin [(mean sheath length) \times (number of sheaths per oligodendrocyte)] at DIV14 and DIV21. The number of branches, myelin sheath length, and total myelin sheath per oligodendrocyte were determined using the “Neuroanatomy SNT neuronal tracer” plugin of the Fiji ImageJ software, analyzed from $N = 11$ (DIV14) and $N = 12$ (DIV21) oligodendrocytes from seven spinal cord organotypic cultures. A two-tailed statistical unpaired t test was used; $*p \leq 0.05$. **O**, Immunoblot analysis of MBP and MAG protein levels. Quantification of MBP and MAG levels at DIV21 relative to DIV14 is shown, analyzed from $N = 3$ (DIV14) and $N = 3$ (DIV21) spinal cord organotypic cultures. A two-tailed statistical unpaired parametric t test was used; $*p \leq 0.05$. **P**, mRNA levels of MBP validated by qPCR, analyzed from $N = 5$ (DIV14) and $N = 5$ (DIV21) spinal cord organotypic cultures. A two-tailed statistical Mann–Whitney test was used; $*p < 0.05$.

- synthesis in oligodendrocyte precursor cells. *Cell calcium* 60:322–330.
- Giorgi C, Marchi S, Pinton P (2018) The machineries, regulation and cellular functions of mitochondrial calcium. *Nat Rev Mol Cell Biol* 19:713–730.
- Grødem S, Nymoen I, Vatne GH, Rogge FS, Björnsdóttir V, Lensjø KK, Fyhn M (2023) An updated suite of viral vectors for in vivo calcium imaging using intracerebral and retro-orbital injections in male mice. *Nat Commun* 14:608.
- Hamilton NB, Clarke LE, Arancibia-Carcamo IL, Kougioumtzidou E, Matthey M, Káradóttir R, Whiteley L, Bergersen LH, Richardson WD, Attwell D (2017) Endogenous GABA controls oligodendrocyte lineage cell number, myelination, and CNS internode length. *Glia* 65:309–321.
- Kirischuk S, Neuhaus J, Verkhatsky A, Kettenmann H (1995) Preferential localization of active mitochondria in process tips of immature retinal oligodendrocytes. *Neuroreport* 6:737–741.
- Krasnow AM, Ford MC, Valdivia LE, Wilson SW, Attwell D (2018) Regulation of developing myelin sheath elongation by oligodendrocyte calcium transients in vivo. *Nat Neurosci* 21:24–28.
- Lu TY, Hanumaihari P, Hsu ET, Agarwal A, Kawaguchi R, Calabresi PA, Bergles DE (2023) Norepinephrine modulates calcium dynamics in cortical oligodendrocyte precursor cells promoting proliferation during arousal in mice. *Nat Neurosci* 26:1739–1750.
- Meyer N, Rinholm JE (2021) Mitochondria in myelinating oligodendrocytes: slow and out of breath? *Metabolites* 11:359.
- Monje M (2018) Myelin plasticity and nervous system function. *Annu Rev Neurosci* 41:61–76.
- Moura DMS, Brennan EJ, Brock R, Cocas LA (2022) Neuron to oligodendrocyte precursor cell synapses: protagonists in oligodendrocyte development and myelination, and targets for therapeutics. *Front Neurosci* 15:779125.
- Narine M, Colognato H (2022) Current insights into oligodendrocyte metabolism and its power to sculpt the myelin landscape. *Front Cell Neurosci* 16:892968.
- Paez PM, Lyons DA (2020) Calcium signaling in the oligodendrocyte lineage: regulators and consequences. *Annu Rev Neurosci* 43:163–186.
- Panattoni G, Amoriello R, Memo C, Thalhammer A, Ballerini C, Ballerini L (2021) Diverse inflammatory threats modulate astrocytes Ca²⁺ signaling via connexin43 hemichannels in organotypic spinal slices. *Mol Brain* 14:159.
- Pitman KA, Young KM (2016) Activity-dependent calcium signaling in oligodendrocyte generation. *Int J Biochem Cell Biol* 77:30–34.
- Powell SK, Khan N, Parker CL, Samulski RJ, Matsushima G, Gray SJ, McCown TJ (2016) Characterization of a novel adeno-associated viral vector with preferential oligodendrocyte tropism. *Gene Ther* 23:807–814.
- Rauti R, Qaisiya M, Tiribelli C, Ballerini L, Bellarosa C (2020) Bilirubin disrupts calcium homeostasis in neonatal hippocampal neurons: a new pathway of neurotoxicity. *Arch Toxicol* 94:845–855.
- Rinholm JE, Vervaeke K, Tadross MR, Tkachuk AN, Kopeck BG, Brown TA, Bergersen LH, Clayton DA (2016) Movement and structure of mitochondria in oligodendrocytes and their myelin sheaths. *Glia* 64:810–825.
- Rone MB, et al. (2016) Oligodendroglialopathy in multiple sclerosis: low glycolytic metabolic rate promotes oligodendrocyte survival. *J Neurosci* 36:4698–4707.
- Rosato-Siri MD, Zoccolan D, Furlan F, Ballerini L (2004) Interneuron bursts are spontaneously associated with muscle contractions only during early phases of mouse spinal network development: a study in organotypic cultures. *Eur J Neurosci* 20:2697–2710.
- Rui Y, Pollitt SL, Myers KR, Feng Y, Zheng JQ (2020) Spontaneous local calcium transients regulate oligodendrocyte development in culture through store-operated Ca²⁺ entry and release. *eNeuro* 7:ENEURO.0347-19.2020.
- Sun XR, Badura A, Pacheco DA, Lynch LA, Schneider ER, Taylor MP, Hogue IB, Enquist LW, Murthy M, Wang SS (2013) Fast GCaMPs for improved tracking of neuronal activity. *Nat Commun* 4:2170.
- Thornton MA, Hughes EG (2020) Neuron-oligodendroglia interactions: activity-dependent regulation of cellular signaling. *Neurosci Lett* 727:134916.
- Wake H, Lee PR, Fields RD (2011) Control of local protein synthesis and initial events in myelination by action potentials. *Science* 333:1647–1651.
- Zhang Y, et al. (2023) Fast and sensitive GCaMP calcium indicators for imaging neural populations. *Nature* 615:884–891.